Bone tissue phantoms for optical flowmeters at large interoptode spacing generated by 3D-stereolithography

Tiziano Binzoni[1,2], Alessandro Torricelli[3], Remo Giust[4], Bruno Sanguinetti[5], Paul Bernhard[6], Lorenzo Spinelli[7]

[1] *Département de Neurosciences Fondamentales, University of Geneva, Switzerland*

[2] *Département de l'Imagerie et des Sciences de l'Information Médicale, University Hospital, Geneva, Switzerland*

[3] *Dipartimento di Fisica, Politecnico di Milano, Milan, Italy*

[4] *Département d'Optique P.M. Duffieux, Institut FEMTO-ST, UMR 6174 CNRS, Université de Franche-Comté, Besançon cedex, France*

[5] *Group of Applied Physics, University of Geneva, Carouge, Switzerland*

[6] *PROFORM AG, Rapid Prototyping, Marly, Switzerland*

[7] *Istituto di Fotonica e Nanotecnologie, Consiglio Nazionale delle Ricerche, Milano, Italy*

tiziano.binzoni@unige.ch

https://sites.google.com/site/humanphotonicsgroup/

Abstract: A bone tissue phantom prototype allowing to test, in general, optical flowmeters at large interoptode spacings, such as laser-Doppler flowmetry or diffuse correlation spectroscopy, has been developed by 3D-stereolithography technique. It has been demonstrated that complex tissue vascular systems of any geometrical shape can be conceived. Absorption coefficient, reduced scattering coefficient and refractive index of the optical phantom have been measured to ensure that the optical parameters reasonably reproduce real human bone tissue in vivo. An experimental demonstration of a possible use of the optical phantom, utilizing a laser-Doppler flowmeter, is also presented.

OCIS codes: (170.0170) Medical optics and biotechnology; (70.3890) Medical optics instrumentation; (170.3340) Laser Doppler velocimetry; (170.1470) Blood or tissue constituent monitoring; (280.2490) Flow diagnostics.

References and links

1. G. Soelkner, G. Mitic, and R. Lohwasser, "Monte Carlo simulations and laser Doppler flow measurements with high penetration depth in biological tissuelike head phantoms," Appl Opt **36**, 5647–5654 (1997).
2. R. Lohwasser and G. Soelkner, "Experimental and theoretical laser-Doppler frequency spectra of a tissuelike model of a human head with capillaries," Appl Opt **38**, 2128–2137 (1999).
3. R. G. M. Kolkman, E. Hondebrink, R. A. Bolt, W. Steenbergen, and F. F. M. de Mul, "Pulsed-laser doppler flowmetry provides basis for deep perfusion probing," Review of Scientific Instruments **72**, 4242–4244 (2001).
4. T. Binzoni, T. S. Leung, D. Boggett, and D. Delpy, "Non-invasive laser Doppler perfusion measurements of large tissue volumes and human skeletal muscle blood RMS velocity," Phys Med Biol **48**, 2527–2549 (2003).

5. T. Bintoni and D. Van De Ville, "Noninvasive probing of the neurovascular system in human bone/bone marrow using near-infrared light," J. Innov. Opt. Health Sci. **04**, 183–189 (2011).
6. M. Belau, M. Ninck, G. Hering, L. Spinelli, D. Contini, A. Torricelli, and T. Gisler, "Noninvasive observation of skeletal muscle contraction using near-infrared time-resolved reflectance and diffusing-wave spectroscopy," J Biomed Opt **15**, 057007 (2010).
7. G. Yu, T. Durduran, C. Zhou, R. Cheng, and A. G. Yodh, "Near-infrared diffuse correlation spectroscopy for assessment of tissue blood flow," in "Handbook of Biomedical Optics," , D. A. Boas, C. Pitris, and N. Ramanujam, eds. (CRC Press: Boca Raton, 2011), pp. 195–216.
8. R. C. Mesquita, T. Durduran, G. Yu, E. M. Buckley, M. N. Kim, C. Zhou, R. Choe, U. Sunar, and A. G. Yodh, "Direct measurement of tissue blood flow and metabolism with diffuse optics," Philos Trans A Math Phys Eng Sci **369**, 4390–4406 (2011).
9. We consider here only non-invasive optical flowmeters working at large source/detector separation (i.e. 'large interoptode spacing'; e.g. $\geq$ 1.5 cm), allowing measurements deep in the investigated tissues. Flowmeters at short interoptode spacing, working on extremely small volumes, are not considered here because they probably need another technical solution for the phantoms.
10. T. Binzoni, D. Tchernin, J. Richiardi, D. Van De Ville, and J. N. Hyacinthe, "Haemodynamic responses to temperature changes of human skeletal muscle studied by laser-Doppler flowmetry," Physiol Meas **33**, 1181–1197 (2012).
11. Näslund, J. and Pettersson, J. and Lundeberg, T. and Linnarsson, D. and Lindberg, L. G., "Non-invasive continuous estimation of blood flow changes in human patellar bone," Med Biol Eng Comput **44**, 501–509 (2006).
12. T. Binzoni, D. Tchernin, J. N. Hyacinthe, D. Van De Ville, and J. Richiardi, "Pulsatile blood flow in human bone assessed by laser-Doppler flowmetry and the interpretation of photoplethysmographic signals," Physiol Meas **34**, 25–40 (2013).
13. F. Jaillon, S. E. Skipetrov, J. Li, G. Dietsche, G. Maret, and T. Gisler, "Diffusing-wave spectroscopy from head-like tissue phantoms: influence of a non-scattering layer," Opt Express **14**, 10181–10194 (2006).
14. M. Brookes and W. Revell, *Blood supply of bone: scientific aspects* (Springer, 1998).
15. L. Spinelli, A. Rizzolo, M. Vanoli, M. Grassi, P. Eccher Zerbini, R. Pimentel, and A. Torricelli, "Optical properties of pulp and skin in brazilian mangoes in the 540-900 nm spectral range: implication for non-destructive maturity assessment by time-resolved reflectance spectroscopy," (International Conference of Agricultural Engineering, CIGR-AgEng2012, Valencia (Spain), 2012).
16. F. Martelli, S. Del Bianco, A. Ismaelli, and G. Zaccanti, *Light propagation through biological tissue and other diffusive media: theory, solutions, and software* (Washington: SPIE Press, 2009).
17. J. R. Mourant, T. Fuselier, J. Boyer, T. M. Johnson, and I. J. Bigio, "Predictions and measurements of scattering and absorption over broad wavelength ranges in tissue phantoms," Appl Opt **36**, 949–957 (1997).
18. A. Pifferi, A. Torricelli, P. Taroni, A. Bassi, E. Chikoidze, E. Giambattistelli, and R. Cubeddu, "Optical biopsy of bone tissue: a step toward the diagnosis of bone pathologies," J Biomed Opt **9**, 474–480 (2004).
19. Y. Xu, N. Iftimia, H. Jiang, L. Key, and M. Bolster, "Imaging of in vitro and in vivo bones and joints with continuous-wave diffuse optical tomography," Opt Express **8**, 447–451 (2001).
20. P. Farzam, P. Zirak, T. Binzoni, and T. Durduran, "Pulsatile and steady-state hemodynamics of the human patella bone by diffuse optical spectroscopy," Physiol Meas **34**, 839–857 (2013).
21. M. A. Bartlett and H. Jiang, "Effect of refractive index on the measurement of optical properties in turbid media," Appl Opt **40**, 1735–1741 (2001).
22. R. Michels, F. Foschum, and A. Kienle, "Optical properties of fat emulsions," Opt Express **16**, 5907–5925 (2008).
23. F. C. Cheong, K. Xiao, and D. G. Grier, "Technical note: characterizing individual milk fat globules with holographic video microscopy," J. Dairy Sci. **92**, 95–99 (2009).
24. P. B. Canham and A. C. Burton, "Distribution of size and shape in populations of normal human red cells," Circ. Res. **22**, 405–422 (1968).
25. M. D. Waterworth, B. J. Tarte, A. J. Joblin, T. van Doorn, and H. E. Niesler, "Optical transmission properties of homogenised milk used as a phantom material in visible wavelength imaging," Australas Phys Eng Sci Med **18**, 39–44 (1995).
26. R. Jensen, *Handbook of Milk Composition*, Food science and technology international series (Academic Press, 1995).
27. H. Li, L. Lin, and S. Xie, "Refractive index of human whole blood with different types in the visible and near-infrared ranges," (2000).
28. T. Binzoni, T. S. Leung, M. L. Seghier, and D. T. Delpy, "Translational and Brownian motion in laser-Doppler flowmetry of large tissue volumes," Phys Med Biol **49**, 5445–5458 (2004).

1. Introduction

Tissue blood flowmetry based on non-invasive optical techniques, such as laser-Doppler flowmetry (LDF) at large interoptode spacings [1, 2, 3, 4, 5] or diffuse correlation spectroscopy

[6, 7, 8], is a unique tool allowing investigating particular physiological phenomena in humans that are not accessible with other known techniques (see note [9]). In fact, optical flowmeters have the advantage of: 1) being non-invasive; 2) allowing long acquisition times with fast repeated measurements; 3) not inducing psychological stress in the subjects (that may influence the regulatory processes of the investigated vascular system); 4) allowing to work in special environmental conditions (e.g. in water); 5) being capable to work with particular tissues such as the bone, where optical techniques remains the only solution for some specific investigative protocols [5]. In fact, thanks to these unique capabilities, it has been possible for example to realize original investigations on the thermoregulatory processes modulating the blood flow of small muscle masses in humans [10] or to observe blood flow pulsations in human bones [11, 12].

In this frame, one of the technical challenges that remains to be solved is the calibration and the testing of the optical flowmeters with suitable optical phantoms (OP). In fact, it appears that it is extremely difficult to produce an OP that reproduces the complex vascular structure of a biological tissue, where the vessels diameter may vary over many orders of magnitude. Attempts in this direction have been limited until now to OP based on the Brownian movement of liquids with no real vascular structure [13], or to OP containing simple straight canals [2] due to the difficulty of creating complex curved structures with varying diameters.

For these reasons, in the present Note we take a step further in the construction of OPs for optical flowmeters. We give an experimental proof of concept that 3D-stereolitography can be used to reproduce complex geometries simulating a tissue's vascular network. In particular, we will show that the generated OPs may be good models for human bone tissue, for which the need of reliable flow measurements techniques represents a key issue for clinical and experimental purposes [14]. Moreover, it will shown that obtained OPs will allow not only to simulate different blood flows but also different tissue blood contents. In practice, this will be done by: 1) producing a simple demonstrative OP prototype; 2) measuring the main optical parameters of the OP; 3) comparing them with *in vivo* measurements for bone tissue found in the literature; 4) showing a possible utilization of the OP with an optical flowmeter.

2. Material and Methods

2.1. The optical phantom

The OP prototype (size $64.5 \times 64.5 \times 40.5$ mm^3) has been build by using a stereolithography (SLA®) system (Viper si2, 3D Systems Inc., Rock Hill, USA). The material composing the OP is Accura® 25, an epoxy resin simulating white acrylonitrile butadiene styrene (ABS) plastic. The OP geometry has been created using the computer-aided design (CAD) software Autodesk® Inventor® professional 2013. The OP (Fig. 1) is crossed by 3 canals (diameter $d = 1.5$ mm) running in parallel over $N = 12$ layers. Each layer, schematically represented in Fig. 2, contains $m = 3 \times 5$ canals. The distance both between the canals and between the layers is 1.5 mm. The distance of the first layer from the upper surface, were the optical fibres of optical flowmeters are placed for the measurements, is 1.5 mm. In this manner the canals form a usable uniform region, in the central part of the OP, of $43.5 \times 43.5 \times 34.5$ mm^3. The percent volume (f) occupied, in the usable region, by the resulting canal network, can be estimated as:

$$f = \frac{m[(d/2)^2\pi][(2m+1)d]N}{[(2m+1)d]^2[2d]N}100 = \frac{1}{8}\frac{m\pi}{2m+1}100 \approx 19.00\%. \quad (1)$$

Intuitively, this means that using 3, 2 or 1 canal (see below) is equivalent to have a 'tissue blood volume' of 19.00%, 12.67% and 6.34%, respectively.

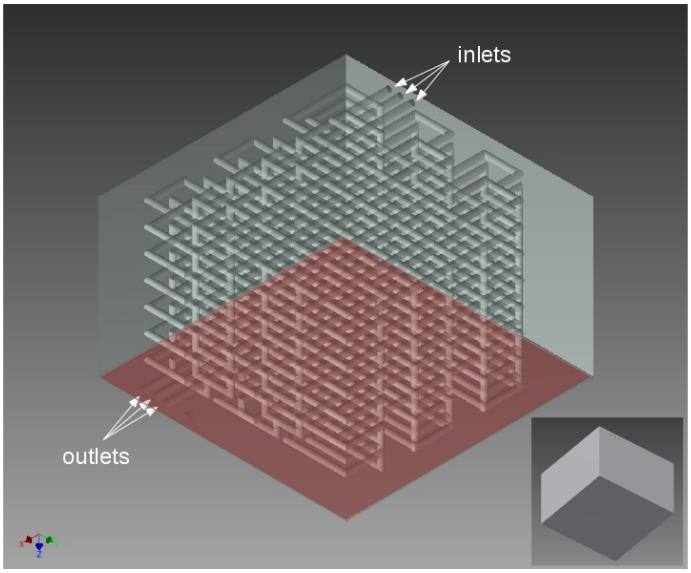

Fig. 1. Transparent view of the OP. The red region highlight the bottom part of the phantom. The real colour of the OP is white and the geometrical appearance is similar to the inset appearing at the bottom-right of the figure. Tubing for the circulation of liquids simulating the ‘tissue blood flow’ are connected to the ‘inlets’ and ‘outlets’.

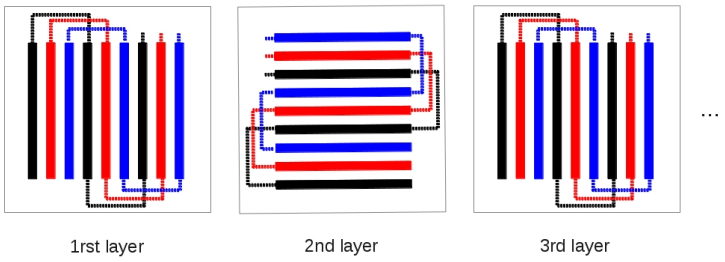

Fig. 2. Intuitive schematic drawing representing the different layers forming the phantom (for clarity the number of canals and dimensions do not correspond to the reality). Each layer is alternatively rotated by 90 degree compared to the following layer. Black, red and blue colours distinguish the 3 canals. Thin lines represent the connections allowing to form a unique long canal for each colour (in the real phantom they move in the 3rd dimension to prevent intersections between canals). The connections between layers are not represented (see Fig. 1 for a complete view).

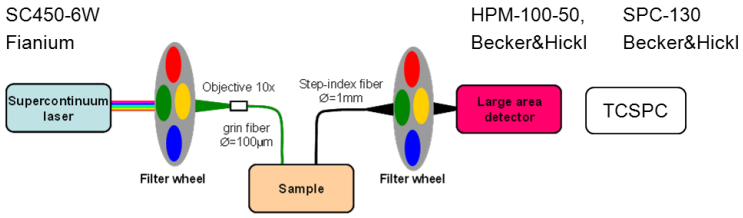

Fig. 3. Schematic drawing representing the time-resolved reflectance spectroscopy setup.

2.2. *The LDF (optical flowmeter)*

The set of measurements allowing to demonstrate a possible OP utilization was realized with a previously described [4, 5] LDF at large interoptode spacing ($r = 1.5$ cm). Summarizing, the LDF consisted of a 785 nm laser source (IRLD50, Moor Instruments Ltd., UK) and a custom made avalanche photodetector (APD) module (Hamamatsu, Japan). A multimode optical fibre, with a cylindric acetal probe head, was connected to the laser. A detection fibre was connected to the APD module with an identical probe head as for the source fibre. All the probes were custom made (Moor Instruments Ltd., UK). The signal (voltage), representing the photo-electric current ($i(t)$) as a function of time (t), was directly acquired from the APD module output by using an analog-to-digital acquisition card (NI USB-6251, National Instruments Corporation, Hungary). The measured parameters, expressed in arbitrary units, were the number ($\bar{n}$) of moving scatterers (e.g. red blood cells) and the flow (Φ). The parameters $\bar{n}$ and Φ were computed as:

$$\bar{n} \propto \langle \omega^{(0)} \rangle / i_0^2, \tag{2}$$

$$\Phi \propto \langle \omega^{(1)} \rangle / i_0^2, \tag{3}$$

where i_0^2 is the mean photo-electric current, and $\langle \omega^{(0)} \rangle$ and $\langle \omega^{(1)} \rangle$ are the 0th and 1st moments of the power density spectrum of $i(t)$.

2.3. *Time-resolved reflectance spectroscopy*

The absortption (μ_a) and reduced scattering (μ_s') coefficients' values of the material composing the OP were assessed by time-resolved reflectance spectroscopy (TRS) on a $20 \times 20 \times 20$ mm^3 sample. The TRS setup (see Fig. 3) was previously developed at the Politecnico di Milano [15]. Shortly, a supercontinuum fiber laser (SC450-6W, Fianium, UK) providing white-light picosecond pulses, adjustable in power by a variable neutral-density attenuator, was utilized as a light source. A filter wheel loaded with 14 band-pass interference filters, was used for spectral selection in the range 540–940 nm. Light was delivered to the sample by means of a multimode graded-index fibre. Diffuse remitted light was collected by a second optical fibre. Then, the light was detected with a photomultiplier (HPM-100-50, Becker&Hickl, Germany) and the photon distribution of time-of-flight was measured by a time-correlated single-photon counting board (SPC-130, Becker&Hickl, Germany). The optical properties in the 540–900 nm spectral range were measured by means of the TRS set-up with the fibres set perpendicularly on two opposite faces. A model for photon diffusion in turbid cubic media was used to analyze TRS data to assess the optical properties of the sample [16].

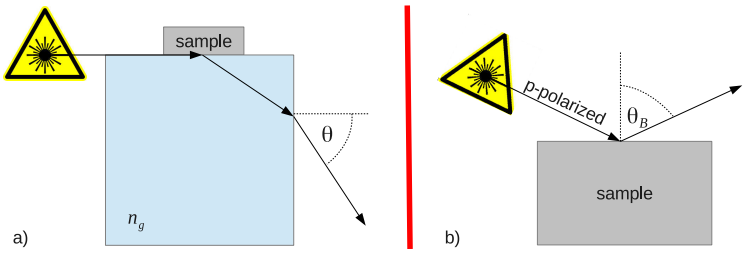

Fig. 4. Schematic drawing representing the two instruments used to measure the refractive index (n) of the different materials. The parameter n_g is the known refractive index of the glass cube (represented in cyan). The parameters θ and θ_B are the measured angles. a) The Pulfrich refractometer; b) The Brewster-angle refractometer.

2.4. Refractometry

2.4.1. Pulfrich refractometer.

A Pulfrich refractometer (Fig. 4a) has been used to estimate the refractive index (n) of the fluids utilised for the LDF demo measurements (Section 2.5). Three different laser sources have been used to perform n measurements at 650 nm, 780 nm and 850 nm. To observe wavelengths out of the visible range the refractomer was equipped with a digital camera (UI-1540SE, IDS, Germany). The parameter n was computed as:

$$n = \sqrt{n_g^2 - \sin^2(\theta)} \tag{4}$$

where θ is the measured angle of refraction and n_g the known glass cube refractive index of the Pulfrich. The refractive index of air was set to 1.

2.4.2. Brewster-angle refractometer.

A Brewster-angle refractometer (Fig. 4b) has been used to estimate the n of the solid material composing the phantom (same cubic sample utilised in Section 2.3). Two polarized laser sources have been used in this case to perform n measurements at 650 nm and 780 nm. The refractometer was equipped with the same type of camera used with the Pulfrich refractometer. The refractive index was computed as:

$$n = \tan(\theta_B) \tag{5}$$

where θ_B is the Brewster-angle. The refractive index of air was set to 1.

2.5. Flow measurements on the OP with LDF

2.5.1. Perfusion system.

A peristaltic pump (minipuls 2, Gilson, France) has been connected with 3 tubing circuits to the OP (Fig. 5). Diluted homogenized fresh cow milk (3.9% fat content) was used as scattering liquid to perfuse the canals. In each of the 3 circuits it was possible to flow independently bi-distilled water or diluted milk. The dilution was 3 ml of milk in bi-distilled water for a total of 500 ml of water-milk mixture. Thanks to the presence of 'droplets' (see below) milk can simulate fluids, containing scatterers, such as human blood [2]. Calibration of the pump was performed for each canal, by directly measuring at the OP outlets the outflowing liquid as a function of time.

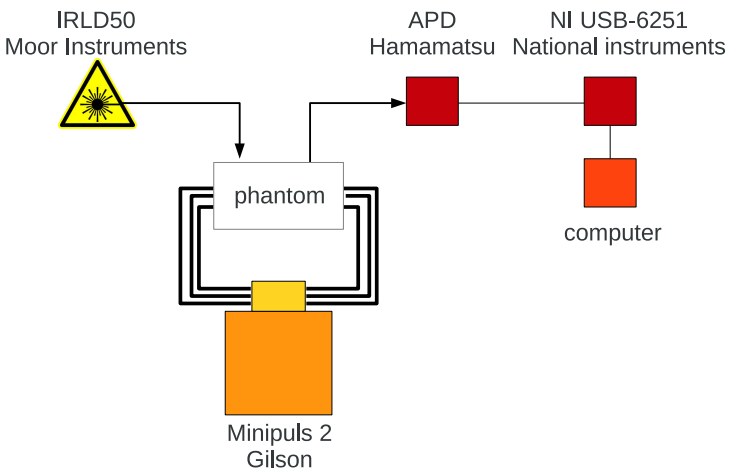

Fig. 5. Schematic drawing representing the experimental setup for testing the OP with an LDF.

2.5.2. Demo measurements with the LDF.

The LDF optodes were placed perpendicularly to the upper OP face, and centred along its diagonal. The LDF measurements (Fig. 5) were obtained by varying the 'real' flow, Φ_{ref}, in the interval 0 and 4 ml min^{-1} and by assessing Φ and $\bar{n}$ with the LDF instrument. The number of flowing scatterers was also varied by using 3, 2 or 1 canal (corresponding to f values 19.00%, 12.67% and 6.34%, see Section 2.1). The non-utilized canals were filled with no-flowing distilled water.

3. Results

Figure 6 shows the μ_a of the material utilised to build the phantom as a function of the wavelength (λ). Each point is the mean of 10 measurements. Considering that there is no recognized mathematical model describing these data a spline interpolation has been used. The red and blue lines show the μ_a values computed with different n values. This, to show the possible range of error (worst case) generated by a wrong n choice when applying the model for photon diffusion in turbid cubic media to the TRS data (see Section 2.3).

The measured n values for the OP material were 1.49 and 1.52 for 650 nm and 780 nm, respectively. The precision of the instrument was $\pm$ 0.05. The value $n = 1.49$ has been chosen for the μ_s' and μ_a estimation for all λ (see Section 4).

Figure 7 shows the μ_s' of the same material analysed in Fig. 6 as a function of λ. Each point is the mean of 10 measurements. Under the simplifying hypothesis that the scattering centres are homogeneous spheres behaving individually (Mie theory), the relationship between μ_s' and λ has been empirically described as [17]:

$$\mu_s' = a\left(\frac{\lambda}{\lambda_0}\right)^{-b}, \tag{6}$$

where $\lambda_0 = 500$ nm; $a = 25.40$ cm^{-1} and $b = 1.37$ have been fitted to the experimental data by non-linear least square regression.

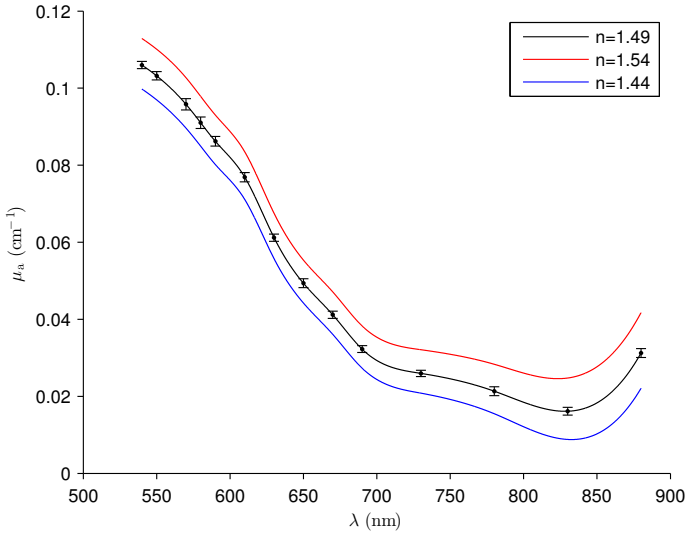

Fig. 6. Absorption coefficient (μ_a) as a function of the wavelength (λ) of the material utilized to build the optical phantom (OP). Vertical bars are standard deviations. The continuous lines are cubic spline interpolations of the data. Data were estimated by using 3 different refractive index (n) values (see text). For clarity, single experimental points obtained with $n = 1.44$ and $n = 1.54$ are not shown.

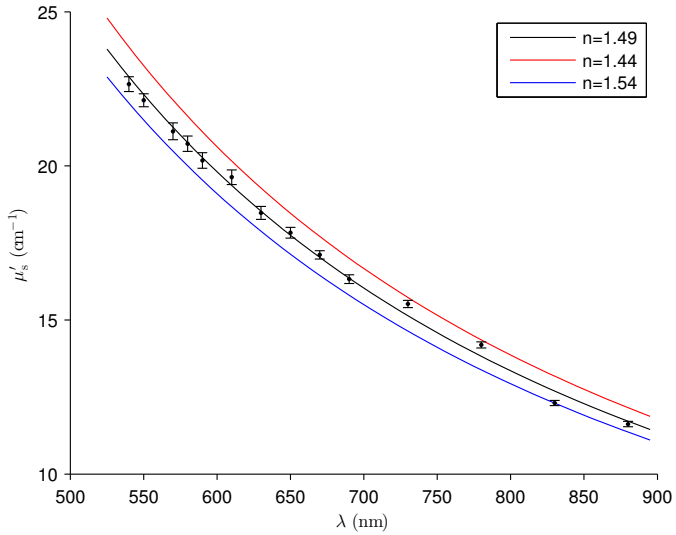

Fig. 7. Reduced scattering coefficient (μ_s') as a function of the wavelength (λ) of the material utilized to build the optical phantom (OP). Vertical bars are standard deviations. The continuous lines were obtained with the model represented by Eq. efeq:model. Data were estimated by using 3 different refractive index (n) values (see text). For clarity, single experimental points obtained with $n = 1.44$ and $n = 1.54$ are not shown.

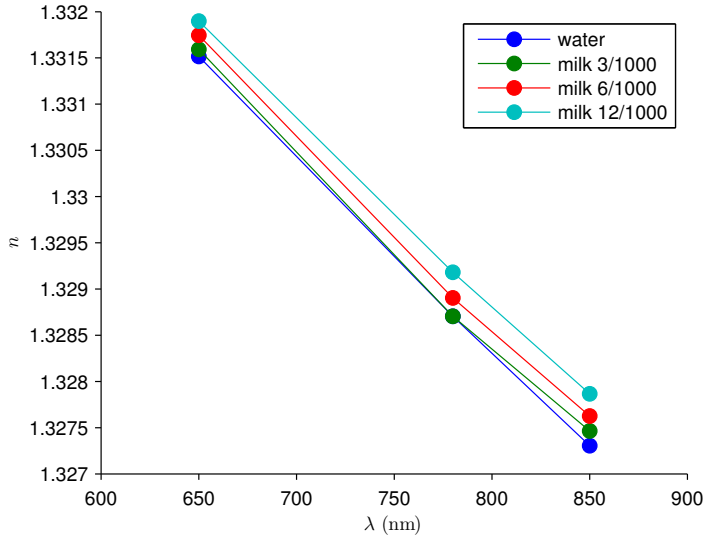

Fig. 8. Refractive index (n) as a function of wavelength (λ) of different milk dilutions in bi-distilled water.

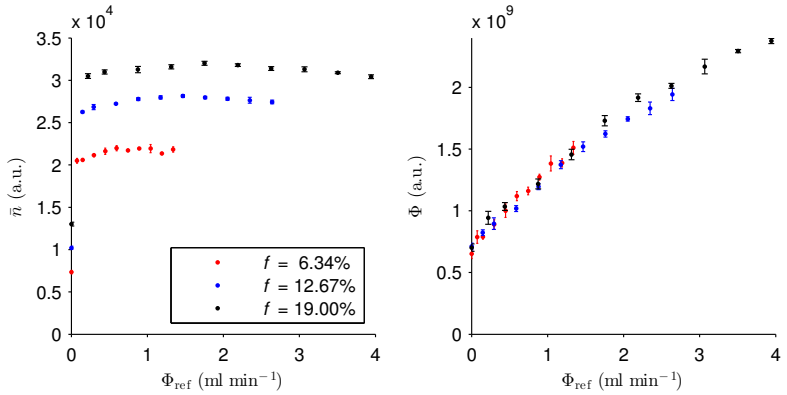

Fig. 9. Measurements of $\bar{n}$ and Φ assessed by LDF. Different colours represent different f values. Vertical bars are standard deviations computed on 5 samples.

As in the case for μ_a, the error induced by the utilization of an approximated n value has been estimated (worst case) and the values are represented by the red and blue lines.

Figure 8 shows n values for bi-distilled water and different milk dilutions in bi-distilled water as a function of λ. As expected, one can see that n increases for increasing the milk concentration and that n decreases as a function of λ.

Figure 9 shows $\bar{n}$ and Φ, assessed by LDF, as a function of Φ_{ref}. As explained in the Material and Methods Section, the parameter Φ_{ref} was varied by changing the fluid volume, f, and/or the fluid speed. The global increase in $\bar{n}$, for a same increase in f, is smaller for a large starting f value; i.e., when going from the blue to the black data. The $\bar{n}$ parameter is non-nil at $\Phi_{\text{ref}} = 0$. This is a typical behaviour of LDF instruments, due to the remaining 'Brownian' movement at

zero flow.

Note that to set $f = 6.34\%$ (i.e. utilization of only 1 canal), anyone of the 3 canals can be chosen because this has no influence on the present measurements (results not shown). The same observation holds for $f = 12.67\%$, where any couple of canals can be chosen.

4. Discussion and conclusions

It has been shown that 3D stereolithography can be used to build OPs for optical flowmeters. Curved canals simulating blood vessel exceeding 2 m in length have been created. For explanatory and testing purposes, the geometrical model that has been chosen was relatively simple, but complex enough to be probably impossible to be created with another technique. For more sophisticated applications, it is easy to build more complex vascular networks, with varying vessels diameter and realistic external shapes (e.g. a bone or a head shape). Any useful geometry can be concieved by means of the CAD software. Images derived from Computed Tomography or Magnetic Resonance Imaging can also be integrated in the CAD design procedure to create even more realistic 3D-printable models. Unlike other 3D printing techniques using ABS, 3D stereolithography allows to create waterproof objects and does, in the present case, not necessitate the use of support material. Impermeability is an essential condition for the present application and the absence of support material during the OP construction is mandatory. In fact, it is not possible to eliminate solid support material from the canals (2 m length and small diameter), even with dedicated solvents, to obtain the finished OP (test not shown here).

The aim of the work was to obtain an OP that reasonably approaches the optical characteristics of *in vivo* human bone tissue. Actually, few groups have measured *in vivo* human bone tissue to assess absolute values of μ_a and μ_s'. Pifferi *et al.* [18] have investigated the calcaneus and found values falling in the range $\mu_a \in [0.05, 0.14]$ cm^{-1} and $\mu_s' \in [11, 16]$ cm^{-1} for $\lambda \in [650, 850]$ nm. Xu *et al.* [19] have measured for the finger bone $\mu_a \in [0.20, 0.25]$ cm^{-1} and $\mu_s' \in [20, 25]$ cm^{-1} for $\lambda = 785$ nm. Farzam *et al.* [20] reported for the patellar bone $\mu_a \in [0.024, 0.071]$ and $\mu_s' \in [3.5, 9.2]$ cm^{-1} for $\lambda \in [690, 830]$ nm). The differences observed in these studies are probably due to differences in the bone structure and to the varying percentage of blood content. By comparing the μ_a and μ_s' values appearing in figures 6 and 7 with the large range of μ_a and μ_s' values found *in vivo*, one can say that the OP prototype can represent a reasonable bone phantom.

The parameters μ_a and μ_s', have been assessed (fitting procedure) by using $n = 1.49$ for all λ because the precision of the refractometer was not sufficient to detect the eventual λ-dependence. As observed by Bartlett and Jiang [21], the chosen n value may influence μ_a and μ_s' estimation. This observation was obtained for a semi-infinite medium, a geometry different from the used cubic OP sample. For this reason the influence of n on the estimation of μ_a and μ_s' has been evaluated for the cubic geometry. The results, appearing in Fig. 6 and 7, show that μ_a and μ_s' remains in a range always suitable to reasonably represent *in vivo* measurements even for large n errors.

For LDF demo it has been necessary to find a fluid able to simulate blood tissue. While the definition of the best blood tissue phantom is far from the aim of the present Note, this topic deserves a comment. Real blood is not practical to be used to perform routine tests on OPs for optical flowmeters. Large quantities of cheap and easy-accessible blood substitutes are in this sense of great interest. Diluted homogenized whole cow milk has been chosen in the present study as blood tissue phantom [2]. Homogenized milk seems to be at first sight a very crude blood phantom, but actually it might have some interesting characteristics compared to other synthetic fat emulsions (e.g. Clinoleic®, Lipovenoes® and Intralipid®) that could be utilized for the same purpose. In fact, the cited emulsion have a mean particle diameter ranging approximatively from 0.08 μm to 0.17μm (estimated from [22]) depending on the brand. Homogenized

whole milk has a mean particle diameter of 1.386 μm [23], a factor of 10 larger than synthetic fat emulsions. This is more closer to the 'mean dimensions' of human red blood cells evolving in the vascular network that is of the order of μm [24]. Other potentially interesting characteristics of homogenized milk (compared also to fresh milk) are its consistency and its stability, as a suspension, over periods of hours when diluted with water [25]. Moreover, the presence of a milk lipid globule membrane covering milk particles [26] adds mechanical stability to them during circulation in the OP and helps to conserve particle number. Due to the utilized high milk-water dilution, the resulting n (Fig. 8) is lower than that for whole human blood [27], which is equal to 1.3776, 1.3702 and 1.3680 for 650 nm, 785 nm and 850 nm, respectively. However, the problem will remains the same also for the above cited blood tissue phantoms alternatives (also due to the high dilution of particles that should be utilized). Thus, milk phantoms simulating blood tissue might also be an interesting solution and probably deserves future investigations.

The LDF measurements shown in Fig. 9 describe a possible utilization of the phantom. In this case, one can appreciate for example the sensitivity of the LDF to the number of moving particle $\bar{n}$. One can see that the $\bar{n}$ increase for increasing f is not strictly linear. In fact, f values of 12.67% or 19.00% are very high compared to a biological tissues (e.g. a skeletal muscle has $f \approx 7\%$), and in this conditions the LDF at large interoptode spacings may have a non-linear behaviour [28], confirmed by the present observations. A slight non-linearity for the Φ measurements appearing for very high Φ_{ref} values is also visible (we did not perform a numerical evaluations because out of the scope of the contribution). Finally, as expected, one can clearly see that Φ changes can be coherently be detected independently that Φ_{ref} changes are obtained by varying the flow speed at constant volume (constant f, i.e. same number of canals) or by varying the the volume at constant speed.

In conclusion, we have shown that the proposed OP prototype clearly opens the possibility to finely test the behaviour of optical flowmeters at large interoptode spacing or to evaluate the quality of the mathematical algorithms implemented in their hardware. Of course in the future, more complex OPs can be conceived allowing for example a largest and finest choice of f values with more sophisticated vascular networks.

Acknowledgments

The research leading to these results has partially received funding from the European Community's Seventh Framework Programme (INFRA-2011-1.1.19. Laser sources) under grant agreement n 284464 (LASERLAB-EUROPE - The Integrated Initiative of European Laser Research Infrastructures III).